



ELSEVIER

Contents lists available at ScienceDirect

Optics Communications

journal homepage: [www.elsevier.com/locate/optcom](http://www.elsevier.com/locate/optcom)

# Optical bistability and free carrier dynamics in graphene–silicon photonic crystal cavities

Tingyi Gu<sup>a</sup>, James F. McMillan<sup>a</sup>, Nicholas W. Petrone<sup>b</sup>, Arend van der Zande<sup>b</sup>, James C. Hone<sup>b</sup>, Mingbin Yu<sup>c</sup>, Guo-Qiang Lo<sup>c</sup>, Dim-Lee Kwong<sup>c</sup>, Chee Wei Wong<sup>a,\*</sup>

<sup>a</sup> Optical Nanostructures Laboratory, Center for Integrated Science and Engineering, Solid-State Science and Engineering, and Mechanical Engineering, Columbia University, New York, NY 10027, United States

<sup>b</sup> Mechanical Engineering, Columbia University, New York, NY 10027, United States

<sup>c</sup> Institute of Microelectronics, Singapore 117685, Singapore

## ARTICLE INFO

### Article history:

Received 5 August 2013

Received in revised form

18 October 2013

Accepted 21 October 2013

Available online 4 November 2013

### Keywords:

Graphene optoelectronics

Bistability

Oscillation

## ABSTRACT

We introduce graphene–silicon hybrid nonlinear devices operating at a few femtojoule cavity circulating energies, including: (1) dual- and single-cavity optical bistability; (2) detailed and broadband switching dynamics, and (3) free-carrier and thermal effects in regenerative oscillations. Sub-wavelength nanostructures confine light in a single mode silicon resonator with high  $Q/V$  ratio, enabling strong light interaction with the graphene cladding layer.

© 2013 Elsevier B.V. All rights reserved.

## 1. Introduction

The unique photonic properties of graphene – optical transparency, broadband dispersionless nature, large carrier mobility, and atomic layer thin structure – make it a unique material for integrated photonic devices. Graphene has been examined for its gate-variable optical transitions [1,2] toward broadband electro-absorption modulators [3] and photoreceivers [4,5] including planar microcavity-enhanced photodetectors [6,7], as well as saturable absorption for mode-locking [8]. Third-order nonlinear susceptibility for graphene is reported as large as  $|\chi^{(3)}| \sim 10^{-7}$  esu [9], along with two-photon absorption (TPA) rate five orders of magnitude higher than silicon [10] and large nonlinearities in the terahertz [11]. Coupled with TPA-generated free carrier and consequently thermal dynamics, a wavelength-scale localized photonic crystal cavity enables ultralow power optical bistable switching and self-induced regenerative oscillations at femtojoule cavity energies on the semiconductor chip platform [12]. Here we transfer single layer graphene on suspended silicon photonic crystal membranes and examine the optical bistability and the carrier/thermal-nonlinearity-induced regenerative oscillations on-chip. The refractive index change for the hybrid media, induced by TPA generated free carriers, is twenty times larger than the

monolithic sample, and thus significantly reduces the optical pump power [27].

## 2. Effective two photon absorption in graphene–Si system

The two-photon absorption coefficient  $\beta_2$  in monolayer graphene is estimated through the second-order interband transition probability rate per unit area as [10]

$$\beta = \frac{4\pi^2}{\epsilon_\omega \omega^4 \hbar^3} \left( \frac{v_F e^2}{c} \right)^2, \quad (1)$$

where  $v_F$  is the Fermi velocity,  $\hbar$  is reduced Planck's constant,  $e$  is the electron charge, and  $\epsilon_\omega$  is the permittivity of graphene at the drive frequency. For our 1550 nm wavelengths,  $\beta_2$  for single layer graphene is determined through  $z$ -scan measurements and first-principle calculations to be in the range of  $\sim 3000$  cm/GW [10], compared to 0.8 cm/GW in silicon.

In the hybrid photonic crystal–graphene structure, most of light is confined in the 250 nm silicon membrane, and evanescently coupled to the  $\sim 1$  nm graphene cladding layer (Fig. 1). The effective TPA coefficient is a balance between graphene and silicon, weighted by the optical field distributions. The effective two-photon absorption coefficient of graphene on silicon is

\* Corresponding author. Tel.: +1 212 854 4275.

E-mail addresses: [tg2342@columbia.edu](mailto:tg2342@columbia.edu) (T. Gu), [cww2104@columbia.edu](mailto:cww2104@columbia.edu) (C. Wei Wong).

defined as

$$\bar{\beta}_2 = \frac{\left(\frac{\lambda_0}{2\pi}\right)^d \int n^2(r) \beta_2(r) (|E(r) \times E(r)|^2 + 2|E(r) \times E(r)^*|^2) d^d r}{\left(\int n^2(r) |E(r)|^2 d^d r\right)^2} \quad (2)$$

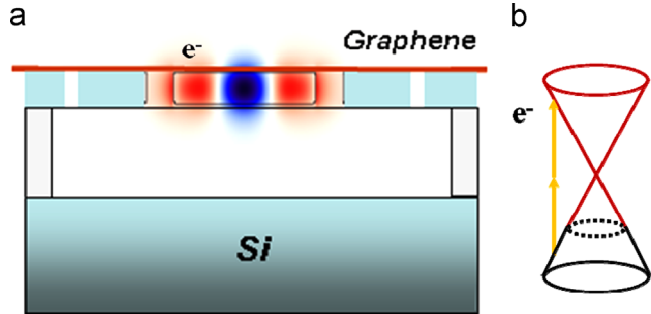


**Fig. 1.** Graphene-cladded silicon photonic crystal cavity. (a) Cross section of the graphene-cladded silicon photonic crystal membrane. The light blue part is silicon. Silicon oxide (grey part) is released under the photonic crystal part. Graphene (red) is transferred on the TE polarized light confined in the resonator. (b) Band diagram of graphene and two-photon absorption of the near-infrared light. (For interpretation of the references to color in this figure legend, the reader is referred to the web version of this article.)

where  $E(r)$  is the complex fields in the cavity and  $n(r)$  is the local refractive index.  $\lambda_0$  is the wavelength in vacuum, and  $d=3$  is the number of dimensions. The complex electric field  $E(r)$  is obtained from the three-dimensional finite-difference time-domain computations of the optical cavity [13]. The local two-photon absorption rate is 1.5 cm/GW in the silicon membrane and  $\sim 3000$  cm/GW for graphene, and the effective  $n^2$  can be analogously calculated.

### 3. Steady-state bistable switching

We measure and model the nonlinear cavity transmissions with time-domain nonlinear coupled-mode theory [14] for the temporal evolution of the cavity amplitude, carrier densities, and effective cavity temperature as described by

$$\frac{da}{dt} = \left(i(\omega_L - \omega_0 + \Delta\omega) - \frac{1}{2\tau_t}\right)a + k\sqrt{P_{in}}, \quad (3)$$

$$\frac{dN}{dt} = \frac{1}{2\hbar\omega_0\tau_{TPA}} \frac{V_{TPA}}{V_{FCA}} |a|^4 - \frac{N}{\tau_{fc}}, \quad (4)$$

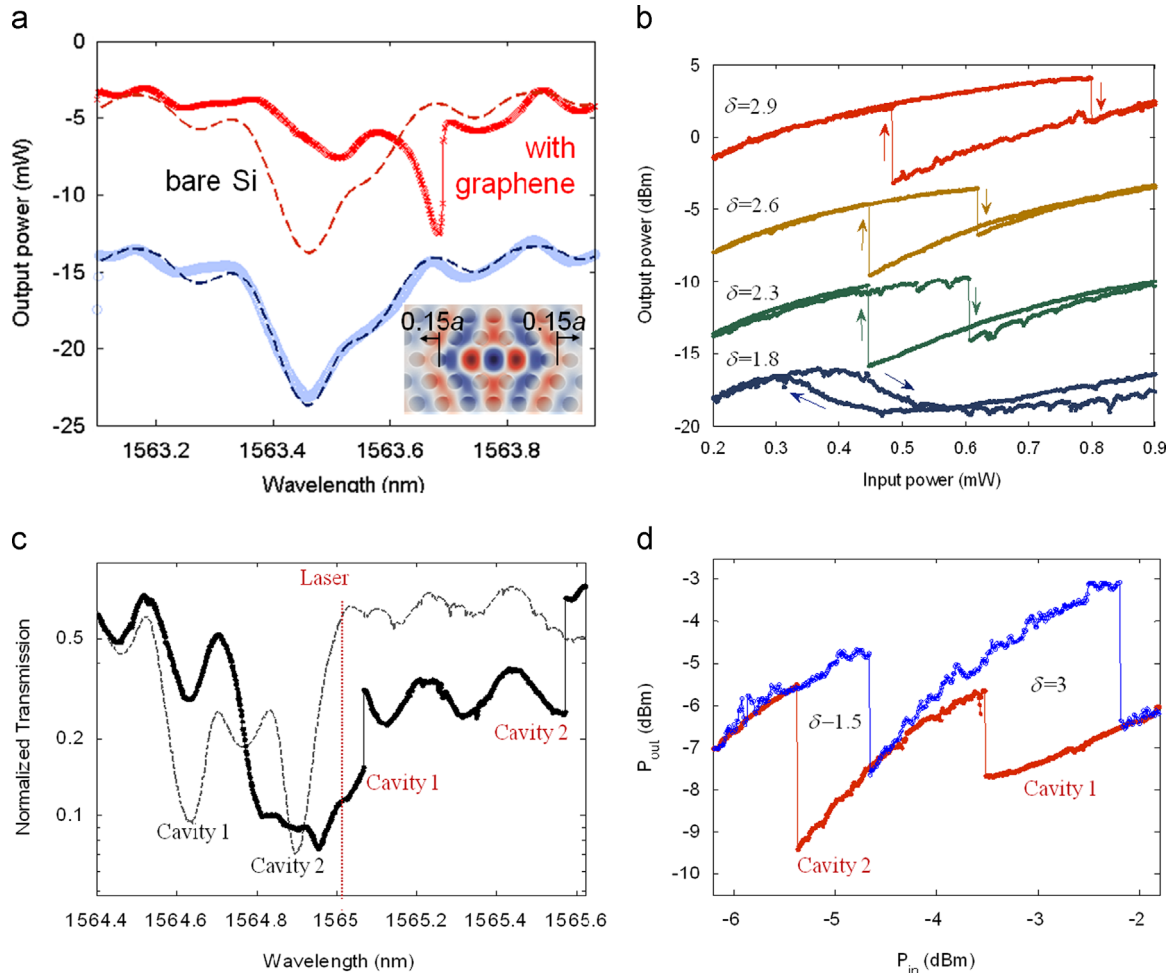


**Fig. 2.** Bistable switching in graphene-clad nanocavities. (a) Measured graphene-cladded cavity transmission with asymmetric Fano-like lineshapes at high power  $P_{in}=0.6$  mW (red dotted line) and low power  $P_{in}=0.1$  mW (blue dotted line). The blue dashed line is coupled mode theory curve fitting in the linear region, with Fano-like interference induced asymmetry. Red dashed line is the coupled mode theory expected transmission lineshape for the same resonance without graphene. Inset: example  $E_z$ -field from finite-difference time-domain computations. (b) Measured steady-state bistability at different detunings set at 0.18, 0.23, 0.26, 0.29 nm (from bottom to top), corresponding to  $\delta=1.8, 2.3, 2.6$  and  $2.9$  ( $\delta=(\lambda_{laser} - \lambda_{cavity})/\Delta\lambda_{cavity}$ ). The plots are offset for clarity: green (offset 2 dB), brown (offset 8 dB) and red lines (offset 15 dB). (c) Normalized transmission of two cavities with resonance separation of  $\delta=3$ . The grey dashed line is measured at  $-16$  dBm input power, and the solid black line is for 0 dBm input. (d) The measured transmission for optical bistability in a two-cavity system as from (c). (For interpretation of the references to color in this figure legend, the reader is referred to the web version of this article.)

$$\frac{d\Delta T}{dt} = \frac{R_{th}}{\tau_{th}\tau_{FCA}} |a|^2 + \frac{\Delta T}{\tau_{th}}, \quad (5)$$

where  $a$  is the amplitude of resonance mode;  $N$  is the free-carrier density;  $\Delta T$  is the cavity temperature shift.  $P_{in}$  is the power carried by incident continuous-wave laser.  $\kappa$  is the coupling coefficient between waveguide and cavity, adjusted by the background Fabry–Perot resonance in waveguide [15].  $\omega_L - \omega_0$  is the detuning between the laser frequency ( $\omega_L$ ) and cold cavity resonance ( $\omega_0$ ). The time-dependent cavity resonance shift is  $\Delta\omega = \Delta\omega_N - \Delta\omega_T + \Delta\omega_K$ , where the free-carrier dispersion is  $\Delta\omega_N = \omega_0 \zeta N/n$ . The thermal induced dispersion is  $\Delta\omega_T = \omega_0 \Delta T (dn/dT)/n$ .  $\Delta\omega_K$  is the Kerr dispersion and, in our scenario, is negligibly small compared to the thermal and free-carrier mechanisms.

The total loss rate is  $1/\tau_t = 1/\tau_{in} + 1/\tau_v + 1/\tau_{lin} + 1/\tau_{TPA} + 1/\tau_{FCA}$ .  $1/\tau_{in}$  and  $1/\tau_v$  is the loss rates into waveguide and vertical radiation into the continuum, ( $1/\tau_{in/v} = \omega/Q_{in/v}$ ), the linear absorption  $1/\tau_{lin}$  for silicon and graphene are demonstrated to be small. The free-carrier absorption rate is obtained from  $1/\tau_{FCA} = c\sigma N(t)/n$ . The field averaged two-photon absorption rate is described by  $1/\tau_{TPA} = c^2/n^2/V_{TPA}|a|^2$ .

The mode volume for two-photon absorption (same as for Kerr) is described by

$$V_{TPA/Kerr} = \frac{(\int n^2(r)|A(r)|^2 dr^3)^2}{\int_{Si} n^4(r)|A|^4 dr^3}, \quad (6)$$

The effective mode volume for free-carrier absorption is

$$V_{FCA}^2 = \frac{(\int n^2(r)|A(r)|^2 dr^3)^3}{\int_{Si} n^6(r)|A(r)|^6 dr^3}, \quad (7)$$

Examining the results in Fig. 2a, the model shows remarkable match to the measured transmissions. With the first-order estimates of the thermal properties (specific heat, effective thermal resistance, and relaxation times), the carrier lifetime of the graphene-clad photonic crystal cavity is estimated to first-order at 200 ps.

Table 1 below summarizes the first-order estimated physical parameters from: (1) coupled-mode theory and experimental data matching; (2) full three-dimensional numerical field simulations, and (3) directly measured data. With the enhanced two-photon absorption in graphene and first-order estimates of the reduced carrier lifetimes, the switching transmission lineshapes for different incident power and cavity energies of the hybrid graphene–silicon cavity are illustrated in Fig. 2a. Due to the partial reflection from the facets of the waveguide, a Fabry–Perot mode is formed in the waveguide, and coupled to the cavity mode [16]. The interference is weak when the extinction ratio of the cavity is large ( $\sim 10$  dB), but the cavity resonance shift due to interference is more significant with decreased extinction ratio at high power due to the induced nonlinear effect. From curve-fitting the

transmission spectrum at low power (linear region), we obtained that waveguide facet reflectivity is  $\sim 0.12$  for a waveguide length of 2 mm.

[CMT]: nonlinear time-dependent coupled-mode theory simulation; [3D]: three-dimensional numerical field calculation averages; [m]: measurement at low power; [cal]: first-order hybrid graphene–silicon media calculations.  $\tau_{fc}$  is the effective free-carrier lifetime accounting for both recombination and diffusion.

With thermal effects, the cavity resonance red-shifts 1.2 nm/mW for the graphene-clad sample ( $Q \sim 7000$ ) and only 0.3 nm/mW for silicon sample (similar  $Q \sim 7500$ ). These sets of measurements are summarized in Fig. 2a where the thermal red-shift is sizably larger in the graphene-clad sample versus a near-identical monolithic silicon cavity. With increasing  $Q$  the monolithic silicon cavity shows an increase in tuning efficiency while the converse occurs for the graphene–silicon cavity. Fig. 2b shows the steady-state bistable hysteresis for controlled and varied detunings. In addition, we examined two side-coupled cavities to the same photonic crystal waveguide [21,22], for dual bistability. Due to the large tunability of the graphene integrated device, double hysteresis loop for two independent cavities with sub-mW inputs (Fig. 2c and d) are observed.

#### 4. Dynamic bistable switching

To verify the bistable switching dynamics, we input time-varying intensities to the graphene-clad cavity, allowing a combined cavity power – detuning sweep. Fig. 3a shows an example time-domain output transmission for two different initial detunings [ $\delta_{(t=0)} = -1.3$  and  $\delta_{(t=0)} = 1.6$ ] and for an illustrative triangular-waveform drive, with nanosecond resolution on an amplified photoreceiver. With the drive period at 77 ns, the observed thermal relaxation time is  $\sim 40$  ns. The dispersive bistable switching is similar to numerical simulations [23]. Cavity resonance dips (with modulation depths  $\sim 3$  dB in this example) are observed for both negative detuning [in the range from  $-0.15$  nm ( $\delta = -0.75$ ) to  $-0.10$  nm ( $\delta = -0.5$ ); Fig. 3b] and positive detuning [up to 0.34 nm ( $\delta = 1.4$ ); Fig. 3c]. With the negative detuning and the triangular pulses, the carrier-induced (Drude) blue-shifted dispersion overshoots the cavity resonance from the drive frequency and then thermally pins the cavity resonance to the laser drive frequency. Since the free carrier lifetime of the hybrid media is about 200 ps and significantly lower than the drive pulse duration, these series of measurements are thermally dominated; the clear (attenuated) resonance dips on the intensity up-sweeps (down-sweeps) are due to the measurement sampling time shorter than the thermal relaxation timescale and a cooler (hotter) initial cavity temperature.

**Table 1**

Estimated physical parameters from time-dependent coupled-mode theory-experimental matching, three-dimensional numerical field simulations, and measurement data.

Parameter	Symbol	GaAs [17]	Si	Monolayer graphene-Si
TPA coefficient	$\beta_2$ (cm/GW)	10.2	1.5 [16,18]	25 [3D]
Kerr coefficient	$n_2$ (m <sup>2</sup> /W)	$1.6 \times 10^{-17}$	$0.44 \times 10^{-17}$ [16,18]	$7.7 \times 10^{-17}$ [3D]
Thermo-optic coefficient	$dn/dT$	$2.48 \times 10^{-4}$	$1.86 \times 10^{-4}$	
Specific heat	$c_{vp}$ (W/Km <sup>-3</sup> )	$1.84 \times 10^6$	$1.63 \times 10^6$ [cal]	
Thermal relaxation time	$\tau_{th,c}$ (ns)	8.4	12	10 [cal]
Thermal resistance	$R_{th}$ (K/mW)	75	25 [19]	20 [cal]
FCA cross section	$\sigma$ (10 <sup>-22</sup> m <sup>3</sup> )	51.8	14.5	
FCD parameter	$\zeta$ (10 <sup>-28</sup> m <sup>3</sup> )	50	13.4	
Carrier lifetime	$\tau_{fc}$ (ps)	8	500 [16,18,20]	200 [CMT]
Loaded Q	Q	7000	7000 [m]	
Intrinsic Q	Q <sub>0</sub>	30,000	23,000 [m]	

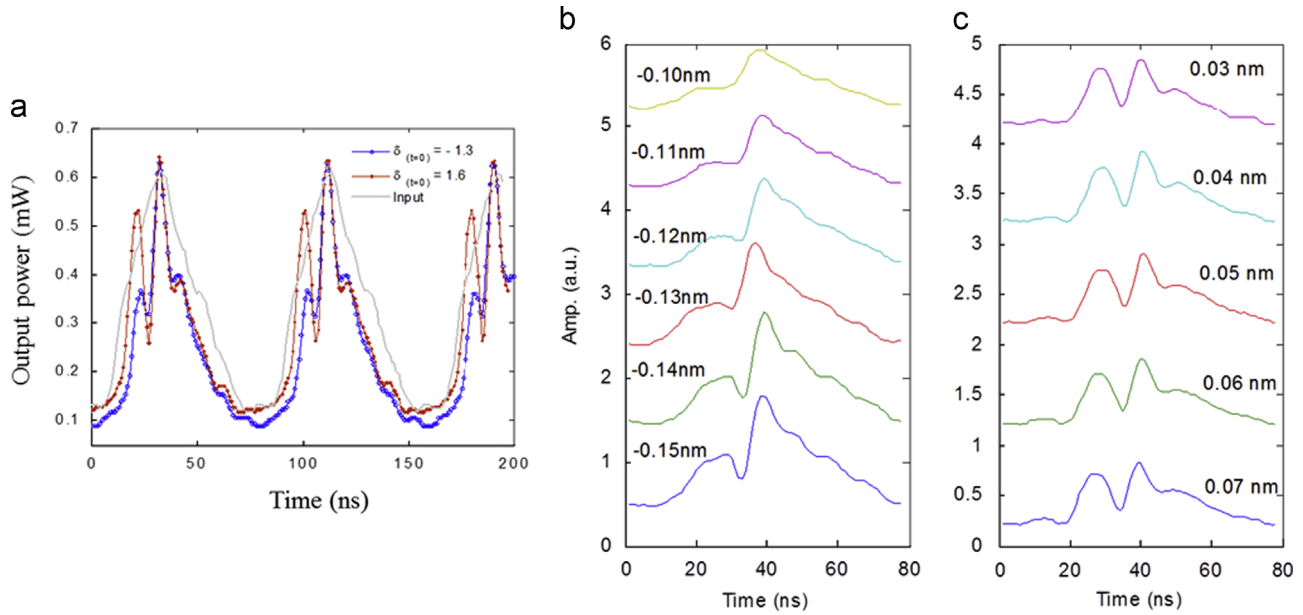


**Fig. 3.** Switching dynamics with triangular waveform drive input. (a) The input experimental waveform is shown in the dashed grey line. The measured bistable resonances are observed for both positive and negative detuning. Blue empty circles:  $\delta_{(t=0)} = -1.3$  ( $\lambda_{\text{laser}} = 1562.10$  nm), red solid circles:  $\delta_{(t=0)} = 1.6$  ( $\lambda_{\text{laser}} = 1562.68$  nm). Inset: schematic of high- and low-state transmissions. (b) The measured output switching dynamics with the input as in (a), at negative detunings (b) and positive detunings (c). Due to limited cavity linewidth, no resonance dips are observed for detunings between  $-0.1$  nm and  $0.03$  nm. (For interpretation of the references to color in this figure legend, the reader is referred to the web version of this article.)

## 5. Regenerative oscillation with thermal and free-carrier nonlinearities

When the input laser intensity is well above the bistability threshold, the graphene-cavity system deviates from the two-state bistable switching and becomes oscillatory. Regenerative oscillation has only been suggested in a few prior studies, such as theoretically predicted in nanocavities with large Kerr nonlinearities [24–27] or observed in high  $Q$  ( $3 \times 10^5$ ) silicon microdisks [28]. These regenerative oscillations are formed between the competing phonon and free carrier populations, with slow thermal red-shifts ( $\sim 10$  ns timescales) and fast free-carrier plasma dispersion blue-shifts ( $\sim 200$  ps timescales) in the case of our graphene-silicon cavities. The self-induced oscillations across the drive laser frequency are observed at threshold cavity powers of  $0.4$  mW, at  $\sim 9.4$  ns periods in these series of measurements which gives  $\sim 106$  MHz modulation rates, at experimentally-optimized detunings from  $\delta_{(t=0)} = 0.68$ – $1.12$ . The graphene-enhanced two-photon absorption, free-carrier and thermal effects allow regenerative oscillations to be experimentally observable with  $Q^2/V$  figure-of-merit values [of  $4.3 \times 10^7(\lambda/n)^3$ ] at least  $50 \times$  lower. The regenerative oscillations with lower  $Q$ s allow higher speed and wider bandwidth operation, and are less stringent on the device nanofabrication [29].

The system transits to the regime of self-sustained oscillations as the power coupled into the cavity is above the threshold. As illustrated in Fig. 4a, the fast free-carrier response fires the excitation pulse (blue dashed line; cycle initiation). Heat diffusion (red solid line) with its slower time constant determines the recovery to the quiescent state in the graphene-cladded suspended silicon membrane. The formal definition of the intrinsic cavity energy  $U_c$  is  $U_c = Q_{\text{intrinsic}} P_l / \omega$ , where  $P_l$  is the power loss from the cavity and  $\omega$  is the excitation frequency [30]. The beating rate between the thermal and free carrier population is around  $50$  MHz, as shown in the inset of Fig. 4b, with the matched experimental data and coupled-mode theory simulation. The beating gives rise to tunable peaks in the radio frequency spectra (Fig. 4b; blue solid line), which are absent when the input power is below the oscillation threshold (grey dashed line). By tuning the laser detunings,

the fundamental mode can be set from  $48$  MHz (zero detuning) to  $55$  MHz ( $0.3$  nm detuning).

The high two-photon absorption in the graphene-silicon hybrid system generates large free-carrier Drude plasma dispersion (negative cavity resonance shift) and large thermal red-shifts from the eventual free-carrier non-radiative recombination (positive cavity resonance shift). Either of the processes is demonstrated to show optical bistability in optical cavities [15,31–34]. Free-carrier dispersion dominates the resonance shift at first instances [35] while thermal red-shift dominates the longer-term response. We use coupled mode theory to separate the negative free carrier dynamics from the positive thermal dynamics, and the effective resonance shift is the combination of the two (Fig. 4c). Kerr nonlinearity induced dispersion is negligible here. Free-carrier and thermal dispersion versus the energy circulating in cavity are shown in left plot of Fig. 4d, while the right plot shows the combined resonance shift oscillations versus cavity energy.

In comparison with different material platforms such as III-V and monolithic silicon, graphene brings about a lower switching energy due to strong two-photon absorption ( $\sim 3000$  cm/GW) [10]. The recovery times of thermal switching (in red) are also shortened due to higher thermal conductivity in graphene, which is measured for supported graphene monolayers at  $600$  W/mK and bounded only by the graphene-contact interface and strong interface phonon scattering.

## 6. Conclusion

Here we describe graphene-silicon hybrid optoelectronic devices operating at a few femtojoule cavity recirculating energies, including ultralow power resonant optical bistability and self-induced regenerative oscillations. These phenomena, in comparison with control measurements on solely monolithic silicon cavities, are enhanced by the dramatically-large  $\chi^{(3)}$  nonlinearities in graphene and the large  $Q/V$  ratios in wavelength-scale photonic crystal cavities. These nonlinear results demonstrate the feasibility

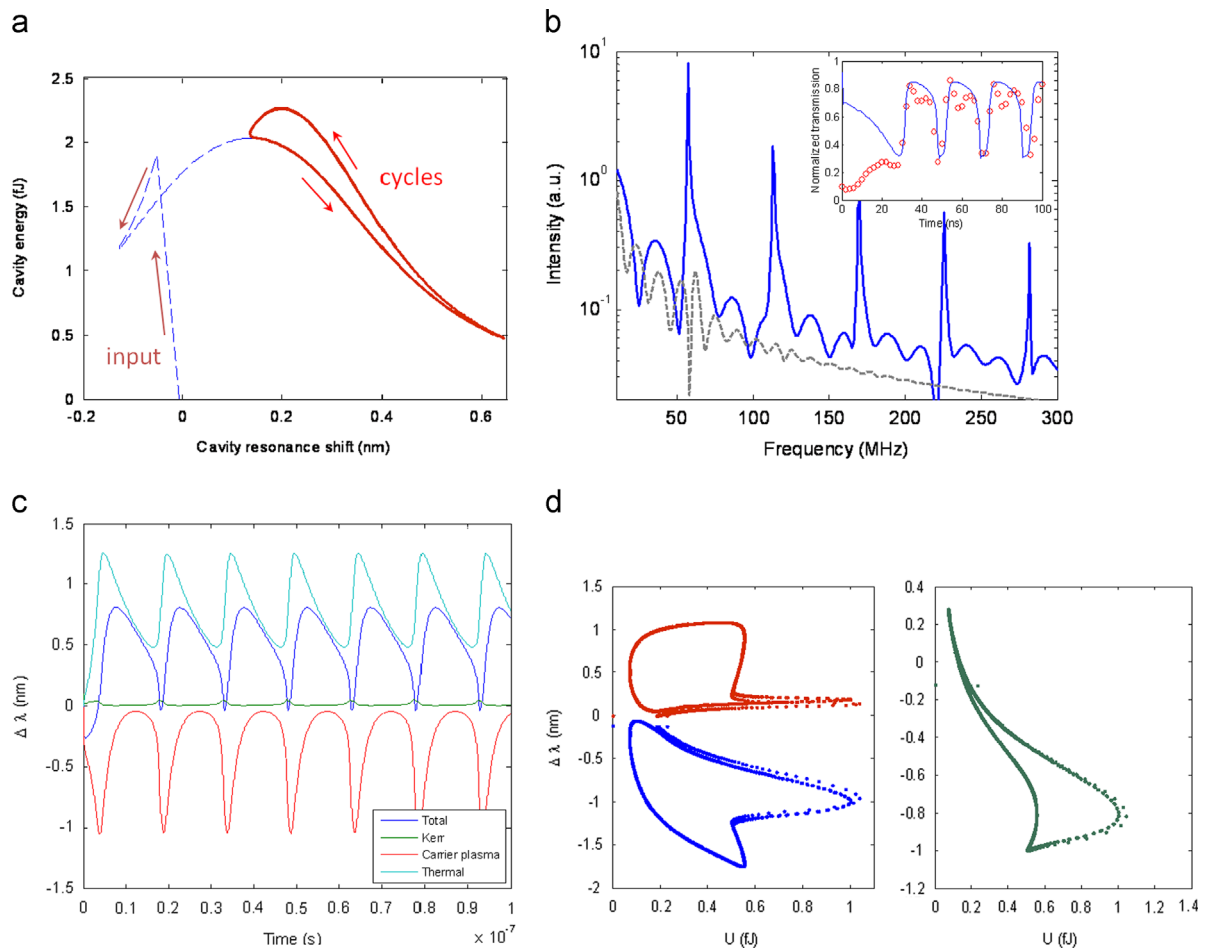


**Fig. 4.** Coupled mode theory calculated cavity resonance oscillation. (a) Nonlinear coupled-mode theory model of cavity transmission versus resonance shift, in the regime of regenerative oscillations. With a detuning of 0.15 nm [ $\delta_{(t=0)}=0.78$ ] the free carrier density swings from  $4.4$  to  $9.1 \times 10^{17}$  per  $\text{cm}^3$  and the increased temperature  $\Delta T$  circulates between 6.6 and 9.1 K. (b) RF spectrum of output power at below (0.4 mW, grey dashed line) and above oscillation threshold (0.6 mW, blue solid line) at the same detuning  $\delta_{(t=0)}=0.78$  ( $\lambda_{\text{laser}} - \lambda_{\text{cavity}}=0.15$  nm). Inset: normalized transmission from model (blue line) and experimental data at the constant power levels (red circles). (c) Cavity resonance shifts due to different nonlinear dispersion versus time. (d) Left plots: Thermal (red) and free carrier (blue) dispersion induced cavity resonance shift versus the energy circulating in cavity. Right plot: the total carrier resonance dispersion versus cavity circulating energy. (For interpretation of the references to color in this figure legend, the reader is referred to the web version of this article.)

and versatility of hybrid two-dimensional graphene–silicon nanophotonic devices for next-generation chip-scale radio-frequency light sources and optical modulators for optical signal processing.

## References

- [1] F. Wang, et al., *Science* 320 (2008) 206.
- [2] Z.Q. Li, et al., *Nat. Phys.* 4 (2008) 532.
- [3] M. Liu, et al., *Nature* 474 (2011) 64.
- [4] T. Mueller, F. Xia, P. Avouris, *Nat. Photon.* 4 (2010) 297.
- [5] F. Xia, et al., *Nat. Nano* 4 (2009) 839.
- [6] M. Engel, et al., *Nat. Commun.* 3 (2012) 906.
- [7] M. Furchi, et al., *Nano Lett.* 12 (2012) 2773.
- [8] Z. Sun, et al., *ACS Nano* 4 (2010) 803.
- [9] E. Hendry, P.J. Hale, J. Moger, A.K. Savchenko, *Phys. Rev. Lett.* 105 (2010) 097401.
- [10] H. Yang, X. Feng, Q. Wang, H. Huang, W. Chen, A.T.S. Wee, W. Ji, *Nano Lett.* 11 (2011) 2622.
- [11] H. Dong, C. Conti, F. Biancalana, *J. Phys. B: At. Mol. Opt. Phys.*, 46, 155401.
- [12] T. Gu, N. Petrone, J.F. McMillan, A. van der Zande, M. Yu, G.-Q. Lo, D.L. Kwong, J. Hone, C.W. Wong, *Nat. Photon.* 6 (2012) 554.
- [13] A.F. Oskooi, D. Roundy, M. Ibanescu, P. Bermel, J.D. Joannopoulos, S.G. Johnson, *Comput. Phys. Commun.* 181 (2010) 687.
- [14] H.A. Haus, *Waves and Fields in Optoelectronics*, Prentice-Hall, Englewood Cliffs, NJ (1984) 99.
- [15] X. Yang, C. Husko, M. Yu, D.-L. Kwong, C.W. Wong, *Appl. Phys. Lett.* 91 (2007) 051113.
- [16] X. Yang, C.W. Wong, *Opt. Express* 15 (2007) 4763.
- [17] A. de Rossi, M. Lauritano, S. Combrì, Q. Vy Tran, C. Husko, *Phys. Rev. A*, 79, 043818.
- [18] A.D. Bristow, N. Rotenberg, H.M. van Driel, *Appl. Phys. Lett.* 90 (2007) 191104.
- [19] C.J. Chen, J. Zheng, T. Gu, J.F. McMillan, M. Yu, G.-Q. Lo, D.-L. Kwong, C.W. Wong, *Opt. Express* 19 (2011) 12480.
- [20] P.E. Barclay, K. Srinivasan, O. Painter, *Opt. Express* 13 (2005) 801.
- [21] S. Kocaman, X. Yang, J.F. McMillan, M.B. Yu, D.L. Kwong, C.W. Wong, *Appl. Phys. Lett.* 96 (2010) 221111.
- [22] T. Gu, S. Kocaman, X. Yang, J.F. McMillan, M.B. Yu, G.-Q. Lo, D.-L. Kwong, C.W. Wong, *Appl. Phys. Lett.* 98 (2011) 121103.
- [23] M.F. Yanik, S. Fan, M. Soljacic, *Appl. Phys. Lett.* 83 (2003) 2739.
- [24] A. Armaroli, et al., *Phys. Rev. A* 84 (2011) 053816.
- [25] V. Grigoriev, F. Biancalana, *Phys. Rev. A* 83 (2011) 043816.
- [26] S. Malaguti, G. Bellanca, A. de Rossi, S. Combrì, S. Trillo, *Phys. Rev. A*, 83, 051802(R).
- [27] S. Malaguti, G. Bellanca, S. Trillo, *Opt. Express* 21 (2013) 15859.
- [28] T.J. Johnson, M. Borselli, O. Painter, *Opt. Express* 14 (2006) 817–831.
- [29] J. Yang, T. Gu, J. Zheng, X. Yang, M. Yu, G.-Q. Lo, D.-L. Kwong, and C.W. Wong, *Opt. Soc. Am.*, 2012.
- [30] J.D. Jackson, *Classical Electrodynamics*, Wiley, Hoboken, NJ 07030, 1999.
- [31] V.R. Almeida, M. Lipson, *Opt. Lett.* 29 (2004) 2387.
- [32] Q. Xu, M. Lipson, *Opt. Lett.* 31 (2006) 341.
- [33] T. Tanabe, M. Notomi, S. Mitsugi, A. Shinya, E. Kuramochi, *Opt. Lett.* 30 (2005) 2575.
- [34] K. Nozaki, T. Tanabe, A. Shinya, S. Matsuo, T. Sato, H. Taniyama, M. Notomi, *Nat. Photon.* 4 (2010) 477.
- [35] C. Husko, A. De Rossi, S. Combrì, Q.V. Tran, F. Raineri, C.W. Wong, *Appl. Phys. Lett.* 94 (2009) 021111.